Computer Modeling in Engineering & Sciences
DOI:10.32604/cmes.2020.011076
Article

Tech Science Press

Effect of Hole Density and Confining Pressure on Mechanical Behavior of Porous Specimens: An Insight from Discrete Element Modeling

Yuanchao Zhang[1], Zhiyuan Xia[2,*], Yujing Jiang[1], Miao Chen[3], Jiankang Liu[1] and Qian Yin[4]

[1]Nagasaki University, Nagasaki, 852-8521, Japan
[2]University of Science and Technology Beijing, Beijing, 100083, China
[3]Shandong University of Science and Technology, Qingdao, 266590, China
[4]China University of Mining and Technology, Xuzhou, 221116, China
[*]Corresponding Author: Zhiyuan Xia. Email: zhiyuanxia1991@126.com
Received: 19 April 2020; Accepted: 09 June 2020

Abstract: Hole-like defects are very common in natural rock or coal mass, and play an important role in the failure and mechanical behaviors of rock or coal mass. In this research, multi-holed coal specimens are constructed numerically and calibrated based on UDEC-GBM models. Then, the strength, deformation and failure behavior of the porous specimens are analyzed, with consideration of hole density (P) and confining pressure (σ_3). The simulation results are highly consistent with those available experiment results, and show that the compressive strength decreases exponentially with the increasing hole density. The strength loss is mainly caused by the reduction of cohesion when $P < P_{cr}$ (critical hole density) and the reduction of frictional angle when $P > P_{cr}$. Also, the increasing hole density linearly reduces the tangent and secant modulus and causes greater nonlinear deformation of multi-holed specimens. Finally, the failure patterns, coalescence mechanism and damage behavior of the multi-holed specimens are revealed based on the analysis of mesoscopic displacement fields and stress distribution around holes. This research promotes a better understanding of the effects of hole density and confining pressure on the failure and mechanical behavior of porous geomaterials.

Keywords: Porous specimen; failure; strength; DEM

1 Introduction

Recent years, underground engineerings have developed rapidly, including both traditional underground engineerings, such as tunnels and mines, and some emerging geothermal engineerings, waste storage engineerings, and CO_2 geological sequestrations etc. However, the development of underground engineerings has also encountered many challenges, most of which are caused by the discontinuity, heterogeneity and anisotropy of geological rock mass. The rock or coal mass always contains various discontinuities: joints, faults, bedding planes and pores or cavities. The disturbance caused by underground excavations may induce crack initiation, propagation and coalescence between these flaws, leading to the instability of surrounding coal and rock mass. In order to study the strength, deformation deterioration and damage mechanism caused by these defects, scholars have used pre-cracked rock-like materials to study the crack

types, coalescence modes and propagation process under uniaxial or triaxial compression [1–8]. As the rock-like materials are very difficult to simulate the heterogeneity, mineral grains, boundary effect and cementation of the real rock materials, many scholars have also studied the cracking behavior of pre-cracked real rock such as sandstone [9,10], marble [11–13], and granite [14,15].

Although the research results are very rich about the strength, deformation and failure mechanism of rock or rock-like materials containing crack-like flaws, there are relatively few studies on hole-like flaws. In fact, on a macroscopic scale, rock materials such as tuff [16], weakly cemented coarse sandstone [17] and some other natural rock masses [18] always contain many macroscopic cavities, as shown in Figs. 1a–1c. On a microscopic scale, rock or coal materials contain very complex pore or hole structures, such as the sandstone [19], Fig. 1d; low-rank coal [20] (coal with a lower degree of coalification, usually has a large and rich pore structure, Fig. 1e) and SC coal [21] (i.e., subbituminous coal, always presenting a significant pore spaces for coalbed methane adsorption, Fig. 1f). In order to explore the effect of hole-like flaws on mechanical behavior of brittle rock materials, Lajtai et al. [22] and Martin [23] studied the fracture around circular opening and observed three types of cracks around the hole i.e., initial cracks, remote (or far-field) cracks and shear cracks. Wong et al. [24] explored the axial splitting failure of one-hole granite samples with various hole diameter and sample width, and concluded that the interaction between hole and sample boundary can promote the tensile cracks propagation along the axial direction. Also, Li et al. [25] applied DIC technique to record and analyze the deformation and fracturing process of one-hole marble specimens. Zeng et al. [26] explored the strength and deformation behavior of brittle sandstone specimens containing different shapes of holes under uniaxial compression. To examine the coalescence and failure behavior between two or more holes, Zhu et al. [27], Huang et al. [28] and Lin et al. [29] have studied the effect of rock bridge length and bridge angle on the crack initiation, coalescence mode and peak strength of specimens. And three basic coalescence modes can be observed in their results: tensile mode, shear mode, and mixed mode by tensile and shear. In addition, the effect of hole density (or macroporosity) on strength and deformation of void-rich rock specimens have been studied based on tuff [16,30–35], sandstone [36–38] and pre-holed plaster specimens [32,33]. Their results showed that the uniaxial compression strength (UCS) and elastic modulus tend to decrease with the increasing macroporosity (or hole density). Although the above experiments can reveal some macroscopic mechanical behavior of rock materials containing void-like flaws, the mesoscopic

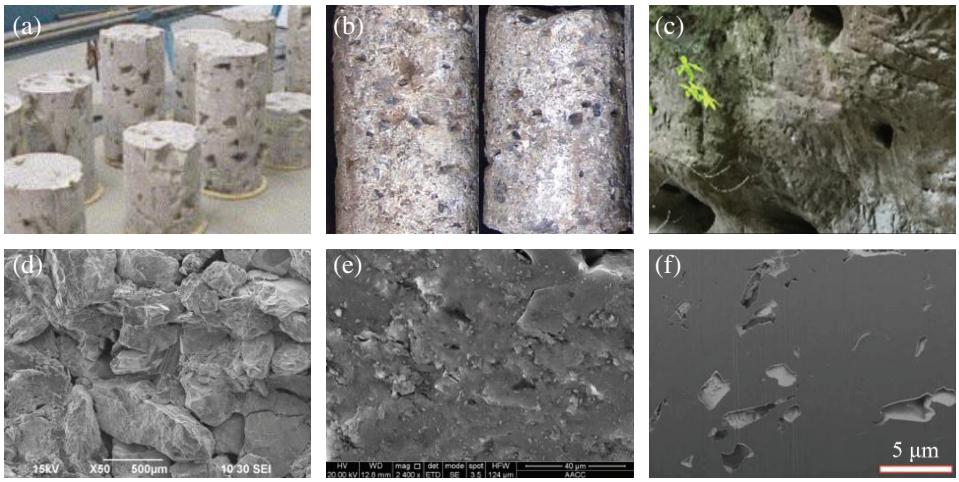

Figure 1: Hole-like flaws in real rock or coal materials. (a) Tuff specimens [16]. (b) Poor cemented coarse sandstone [17]. (c) Natural rock mass [18]. (d) Coarse grain sandstone [19]. (e) Low-rank coal [20]. (f) SC coal samples [21]

coalescence and failure mechanism are still not clear for the powerlessness of those experiments. Besides, the uniaxial compression is difficult to reflect the real in-situ stress state, for overlooking the effect of confining pressure.

Recent years, numerical simulation methods have been increasing applied to rock mechanics and engineerings, especially for the discrete element method (DEM) firstly proposed by Cundall et al. [39]. DEM such as Particle Flow Code (PFC) and Universal Distinct Element Code (UDEC) would provide a deeper insight into the mesoscopic failure mechanism of rock materials by allowing finite displacements, rotations and detachment of discrete bodies [40–42]. Also, DEM has a greater flexibility than test methods in simulating the complex stress or boundary conditions. Compared with the bonded particle models in PFC, the polygonal block models based on Voronoi tessellation in UDEC can provide a more realistic representation of rock micro-structure and better reflect the full contact between grains and interlocking effect. Using the UDEC, Christianson et al. [43] conducted numerical triaxial testing of simulated lithophysal tuff samples to supplement existing uniaxial compression data. Damjanac et al. [16] explored the mehcanical degradation behavior of emplacement drifts with consideration of in situ, thermal, seismic loads and time effect in UDEC. Kazerani et al. [44] presented a formal methodology for parameters calibration in UDEC by simulating a series of uniaxial/biaxial compression and brazilian tension. In which, the ratio of compressive to tensile strength of rock samples is accurately captured. Lan et al. [45] explored the effects of microgeometric heterogeneity, grain-scale elastic heterogeneity and microcontact heterogeneity on micromechanical behavior and macroscopic response of Lac du Bonnet granite based on UDEC-GBM. Gao et al. [46] used breakable grain-based model based on UDEC Trigon to explore the inter-granular and intra-granular failure within sandstone under both compression and direct-shear tests.

In this paper, multi-holed coal specimens are constructed numerically and calibrated based on UDEC-GBM models. A series of uniaxial and triaxial compression tests are firstly performed to calibrate the model parameters to match the macro-response of tested coal specimens. Then, the strength, deformation and damage behavior of multi-holed coal specimens are analyzed with considering the effect of hole density and confining pressure. This research is dedicated to a clear understanding of the effects of hole-like defects on the failure and mechanical behavior of porous coal materials, and provides theoretical basis for some underground engineerings [47,48].

2 Numerical Modelling

2.1 Constitutive Relation of UDEC-GBM

In the UDEC, a rock material is treated as an assembly of discrete blocks. The blocks which can be either rigid or deformable are separated by interfaces which are viewed as contacts. A force-displacement law is applied at the contacts to find the contact force from the known displacement and Newton's second law is applied to calculate the motion of the blocks resulting from the known forces acting on them. Therefore, In UDEC-GBM models, the macroscopic mechanical behavior of materials mainly depends on the mechanical response of the microscopic contacts between the Voronoi blocks. The force-displacement relationship between the contacts obeys the Coulomb slip constitutive model, as shown in Fig. 2. The contact parameters mainly include stiffness parameters (normal stiffness—k_n and shear stiffness—k_s) and strength parameters (cohesion—c^j; friction angle—φ^j; tensile strength—σ_t^j; residual cohesion—c_r^j and residual internal friction angle—φ_r^j). These micro-properties of the block contacts control the mechanical response of the material and the calibration of the micro-properties of the contacts must be carried out prior to use within a specific rock mass model.

Cracks will be initiated at a contact when the stress applied on the contact exceeds either its tensile or shear strength. This represents the fracturing of the rock masses through intact material. In this study, Coulomb slip model is employed for the contacts so that they may fail either in shear or in tension based on the stress inducing failure. In the normal direction of contact, the normal stress σ_n depends on the

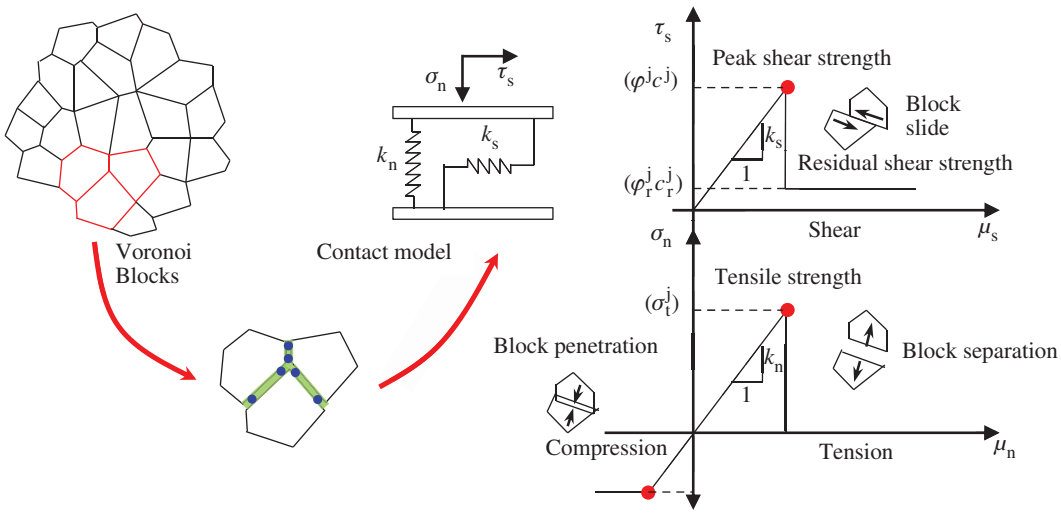

Figure 2: Structure, micro-mechanical properties and constitutive relation of UDEC-GBM

magnitude of normal displacement μ_n and normal stiffness k_n, see Eq. (1) [49]. $\Delta\sigma_n$ is the effective normal stress increment and $\Delta\mu_n$ is normal displacement increment. if $\sigma_n \leq -\sigma_t^j$, then $\sigma_n = 0$. The contact is judged to be tensile failure.

$$\Delta\sigma_n = -k_n \cdot \Delta\mu_n \tag{1}$$

In the tangential direction of contact, tangential stress τ_s is determined by tangential displacement μ_s and tangential stiffness k_s, see Eq. (2) [49]. $\Delta\tau_s$ is tangential stress increment; $\Delta\mu_s^e$ is elastic shear displacement increment. However, the peak shear strength τ_s^{max} of contact is determined by the cohesion c^j and internal friction angle φ^j, see Eq. (3) [49]. When $|\tau_s| \geq \tau_s^{max}$, the contact is determined to be shear failure.

$$\Delta\tau_s = -k_s \cdot \Delta\mu_s^e \tag{2}$$

$$\tau_s^{max} = \sigma_n \tan\varphi^j + c^j \tag{3}$$

Using the UDEC built-in programming language FISH, a function was developed to record the number of shear and tension cracks formed during the simulated tests. A shear crack forms when the shear stress applied on a contact exceeds its shear strength, which is a function of the normal stress, cohesion and friction angle, Eqs. (2) and (3). A tension crack is formed when the normal stress applied on a contact exceeds its tensile strength.

2.2 Establishment of Numerical Specimens

The coal specimens are constructed numerically according to ISRM [50] suggested standard specimen size (width × height = 50 mm × 100 mm), as shown in Fig. 3. The coal specimen is placed between two rigid platens, and the interfaces between platens and specimen are set to frictionless. Considering the modeling uncertainty caused by block size, the numerical specimen is finely divided into small blocks with an average side length of 1 mm, which is accurate enough to achieve stable and repeatable numerical solution, according to Gao et al. [46] and Zang et al. [51]. During the compression, confining pressure (σ_3) is firstly applied, enough calculation steps are necessary to reach the hydrostatic stress state. Then, top platen moves down and the bottom platen is fixed. The loading rate is set to 0.05 'm/s', that is about 1.5×10^{-6} mm/step meaning a slow enough loading rate. During the loading process, the vertical stress

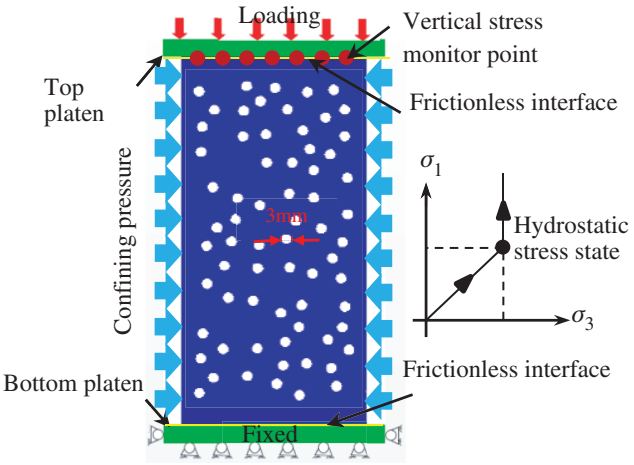

Figure 3: Numerical configurations of multi-holed specimens

(σ_1) is recorded by the monitor points on the top surface, and the vertical strain (ε_1) can be calculated by the vertical displacement of top platen.

In the numerical multi-holed specimens, these holes are uniformly distributed and generated by deleting blocks within a diameter of 3 mm. During the generation of holes, the random number generator is used to generate randomly distributed points in the specimen region, then the blocks around these points will be deleted, until a specified hole density P is met. P is calculated by dividing the total area of holes by the specimen area, see Eq. (4). In addition, There should be enough distance between these random holes to ensure the existence of 'rock bridge'.

$$P = \frac{A_h \times N_h}{A_s} \tag{4}$$

where, P—hole density; A_h—area of a single hole; N_h—number of holes; A_s—area of specimen. Based on the above, the multi-holed specimens with different hole density, i.e., $P = 0$ (intact), $P = 3\%$, $P = 6\%$, $P = 9\%$ and $P = 12\%$, were established.

2.3 Parameters Calibration

For a specific rock material, a unique set of contact parameters can be calibrated so that they satisfy the appropriate material properties including the Young's Modulus, Poisson's ratio, tensile strength, internal friction angle and cohesion. Based on the tests data from Gao et al. [52], micro-parameters calibration is conducted according to the methods suggested by Kazerani et al. [44]. The model parameters in UDEC mainly consists of block parameters (density ρ, bulk modulus K, shear modulus G) and contact parameters showed in Fig. 2. During the calibration process, a method of 'trial and error' is necessary to continuously adjust the microparameters, until the obtained macroscopic strength, deformation and failure pattern are consistent with the test results. The following calibration process is proposed:

(1) Young's modulus was firstly calibrated by varying k_n according to Eq. (5). Both the K and G of blocks are equal to those of real specimens. n is a multiplication factor ($1 \leq n \leq 10$); Δz_{min} is the smallest width of an adjoining zone in the normal direction.

$$\mathrm{k}_n = n \times \frac{\left(K + \frac{4}{3} \times G\right)}{\Delta Z_{\min}} \tag{5}$$

(2) Poisson's ratio was then calibrated by varying k_s/k_n. A relationship supposed by Kazerani et al. [44] can be used for a rapid calibration, see Eq. (6).

$$\frac{k_s}{k_n} = \frac{G}{E} = \frac{1}{2(1+\upsilon)} \tag{6}$$

(3) The tensile strength should be thirdly calibrated by varying the contact tensile strength.

(4) Cohesion and friction angle was finally calibrated by varying the contact cohesion and friction angle. It may be necessary to perform several iterations to match both values.

The calibrated model parameters are shown in Tab. 1. Fig. 4 shows that the numerical stress-strain curves and macroscopic failure patterns are quite similar to test results. The simulated stress-strain curves of intact coal specimens in Fig. 4b are greatly consistent with experimental results in Fig. 4a [52]. Both show an obvious elastic-brittle behavior of intact coal specimens. Also, the triaxial compressive strength (σ_s) increases linearly with increasing confining pressure, the linear regression line is highly coincident with the test results, as shown in Fig. 4c. In addition, the failure under lower confining pressure (σ_3 = 0.5 MPa) shows obvious axial splitting failure, then converts to mixed splitting and shear failure under σ_3 = 2.0 MPa, finally presents a single shear fracture under σ_3 = 3.5 MPa, as shown in Fig. 4d. The high consistency between numerical simulation and test results indicates the reasonability of model parameters used in this research.

Table 1: Calibrated micro-parameters used in UDEC-GBM for coal specimen

	Block			Contact						
Parameters	ρ	K	G	k_n	k_s	c^j	φ^j	c_r^j	φ_r^j	σ_t^j
Units	kg/m^3	GPa	GPa	GPa/m	GPa/m	MPa	°	MPa	°	MPa
Value	1298	2.13	0.95	16982.7	6501.8	9.8	40	0	15	2.0

3 Numerical Simulation Results

3.1 Strength Behavior

Previous studies have showed that the uniaxial compression strength (UCS) of void-rich rock or rock-like materials decreases exponentially with the increasing hole density, no matter for the harder or softer rocks, as shown in Fig. 5a. The numerical results in this research further shows that there is still an approximate exponential relationship between σ_s and P under various confining pressure, as shown in Fig. 5b. To further understand the strength behavior for multi-holed coal specimens, the relationship between triaxial compression strength (σ_s) and confining pressure (σ_3) was presented in Fig. 6a. It can be seen that there is a good linear relationship between σ_s and σ_3. Therefore, the Mohr-Coulomb criteria, described by Eq. (7) [53], can be used to investigate the strength behavior of multi-holed coal specimens.

$$\sigma_s = \sigma_0 + q\sigma_3 = \frac{2c\cos\varphi}{1-\sin\varphi} + \frac{1+\sin\varphi}{1-\sin\varphi}\sigma_3 \tag{7}$$

In Eq. (7), σ_0 represents the uniaxial compressive strength of rock samples; q is a coefficient related to the effect of σ_3 on σ_s. Both σ_0 and q are related to the cohesion c and friction angle φ of materials.

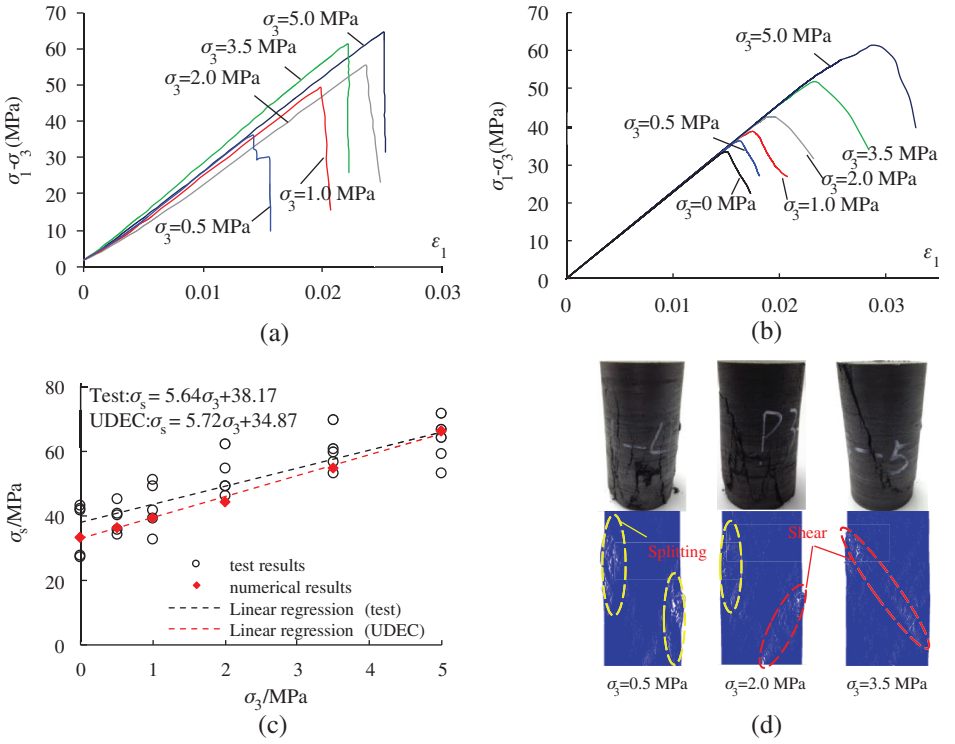

Figure 4: Comparison of strength and failure between numerical simulation and test results [52]. (a) Test results [52]. (b) Numerical results. (c) Linear regression. (d) Failure patterns

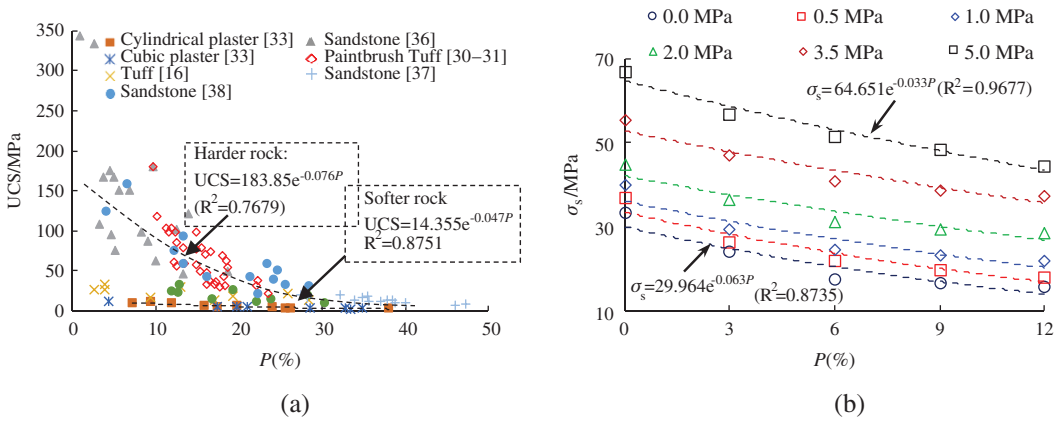

Figure 5: Variations of compressive strength of multi-holed specimens with hole density (a) Variation of UCS with hole density, (b) Variation of triaxial compression strength with hole density

From Fig. 6b, we can see that the increasing hole density firstly causes an obvious decrease of cohesion, then causes the decrease of friction angle. For example, c decreases from 6.44 MPa to 3.44 MPa (fall by 46.5%) when P increases from 0 to 6%, while φ changed not much. When P increases from 6% to 12%, φ decreases from 47.7° to 45.0° and no change has occurred in c. Therefore, the increasing hole density may cause two different damage mechanism, which can be divided by a critical porosity (P_{cr}), i.e., 6% for the multi-holed coal specimens.

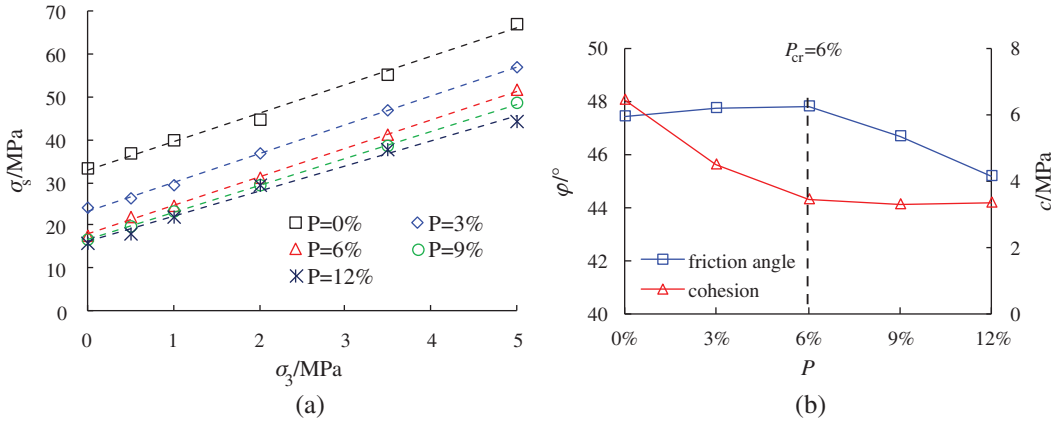

Figure 6: Changes of Mohr-Coulomp parameters with hole density

Based on the Mohr-Coulomp criteria, the strength of rock materials mainly consists of two parts: the inherent cohesive strength and the frictional strength caused by friction effect [54]. Therefore, for multi-hole coal samples, when $P < P_{cr}$, the increasing hole density mainly leads to cohesion strength loss, whereas leading to frictional strength loss when $P > P_{cr}$. Furthermore, the exponential relationship between σ_s and P (see Fig. 5) shows that strength reduction caused by cohesion loss is more greater than by friction loss. For example, the σ_s decreased by 23.1%–48.1% when P increase from 0 to 6% (P_{cr}), while only a reduction by 10.3%–14.2% occurs when P increase from 6% (P_{cr}) to 12%.

3.2 Deformation Behavior

Fig. 7 shows the deviatoric stress-strain curves of multi-holed coal specimens with different hole density (P = 3%–12%) under various confining pressure (σ_3 = 0–5.0 Mpa). Comparing those curves of intact specimens showed in Figs. 4a and 4b, we can find that the pre-peak stage of multi-hole coal specimens contains both linear elastic stage and non-linear stage. Furthermore, the non-linear stage tend to be more obvious with the increasing hole density. To clearly understand the pre-peak deformation behavior, tangent modulus E_t and secant modulus E_s are used to describe the deformation characteristics of multi-holed coal samples, as shown in Fig. 8a. E_t is defined as the slope of linear elastic stage and E_s is defined as the slope of the line connecting the origin and the peak point.

The change of tangent modulus E_t with the hole density under different confining pressure was shown in Fig. 8c. It can be seen that E_t tends to decrease linearly with the increasing hole density under various confining pressure. This result is consistent to the experimental results of Tuff [16,32,34] and pre-holed plaster specimens [32] under uniaxial compression, as shown in Fig. 8b. In addition, Fig. 8c shows that the decreasing rate of E_t is related to the confining pressure. With the increasing σ_3, the decreasing rate of E_t tend to be more smaller. This reflects that the elastic deformation of specimen with higher hole density is more sensitive to confining pressure. However, for the intact specimens (P = 0%), E_t remains unchanged with confining pressure.

Fig. 8d shows that secant modulus E_s is little affected by confining pressure and has a tendency to decrease near-linearly with the increasing hole density. The decreasing rate of E_s is much bigger than that of E_t, indicating that E_s is more sensitive to the hole density than E_t. To describe the degree of nonlinear deformation of pre-peak stage, the values of E_s/E_t are calculated and showed in Fig. 8e. It can be seen that E_s/E_t tend to decrease near-linearly with the increasing hole density, indicating that the degree of non-linear deformation of multi-holed specimens tend to be greater with the increasing hole density. However, Fig. 8f shows that peak strain is mainly affected by confining pressure rather than hole density.

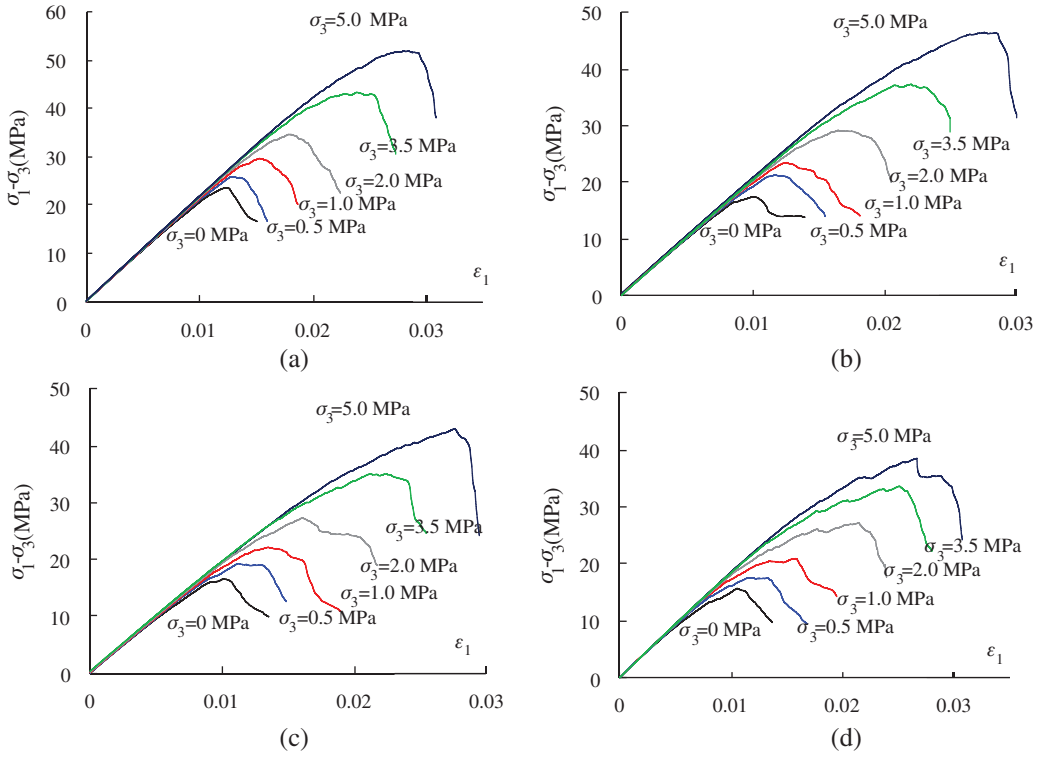

Figure 7: Deviatoric stress-strain curves of multi-holed coal specimens under different confining pressure. (a) P = 3%. (b) P = 6%. (c) P = 9%. (d) P = 12%

ε_p tends to increase linearly with the increasing σ_3, indicating that deformation capability of multi-holed coal specimens tends to be stronger under a higher confining pressure.

The above analysis indicates that both hole density and confining pressure have an significant influence on the deformation behavior of multi-holed coal specimens. The increasing hole density significantly decreases linear elastic deformation, while causes greater nonlinear deformation. However, the deformation capability of multi-holed coal specimen mainly depends on the confining pressure.

3.3 Failure Patterns

Fig. 9 shows the failure patterns of multi-holed coal specimens with different hole density (P) under different confining pressure. Two types of failure modes can be observed in these failed multi-holed specimens.

1. Splitting failure (Mode-I). This mode results from tensile cracks coalescences along the vertical holes. It can only be observed under uniaxial compression.
2. Shear failure along the diagonal tensile coalescence bands (Mode-II). This failure mode involves both tensile cracks coalescence in the bridge areas and shear displacement along the coalescence bands. It is characterized by obviously crushed fragments and holes collapse along the shear planes, and can be observed under various confining pressure.

In order to deeply understand the fracture mechanism of these two types of failure modes, the mesoscopic displacement field was revealed in this research. Fig. 10 shows the mesoscopic displacement of blocks on both sides of the fracture planes. The dense black small arrows in enlarged views represent the magnitude and direction of displacement vector, which is also highlighted by red unfilled arrows

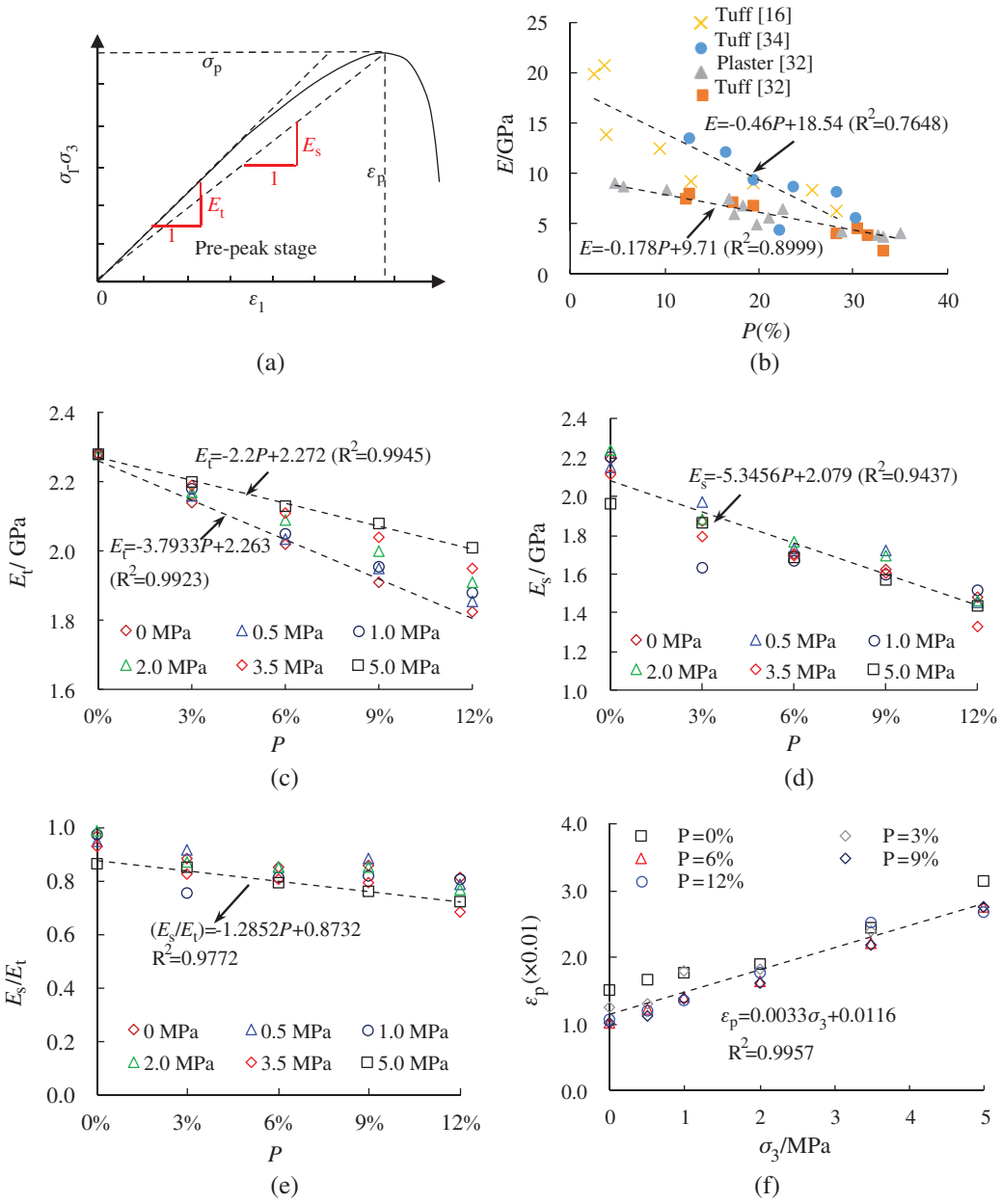

Figure 8: Changes of deformation parameters of multi-holed coal specimens with hole density and confining pressure. (a) Definition of E_s and E_t. (b) Previous tests results. (c) Change of E_t. (d) Change of E_s. (e) Change of E_s/E_t. (f) Change of ε_p

Based on the magnitude and direction of blocks displacement, the relative motion relation between blocks can be identified and the fracture mechanism can be clear. In this research, six types of displacement relationships can be concluded in Fig. 11. S_A and S_B are total displacement vector of blocks, S_A^y and S_B^y are displacement components along the normal direction of fracture plane, S_A^x and S_B^x are components along the tangential direction.

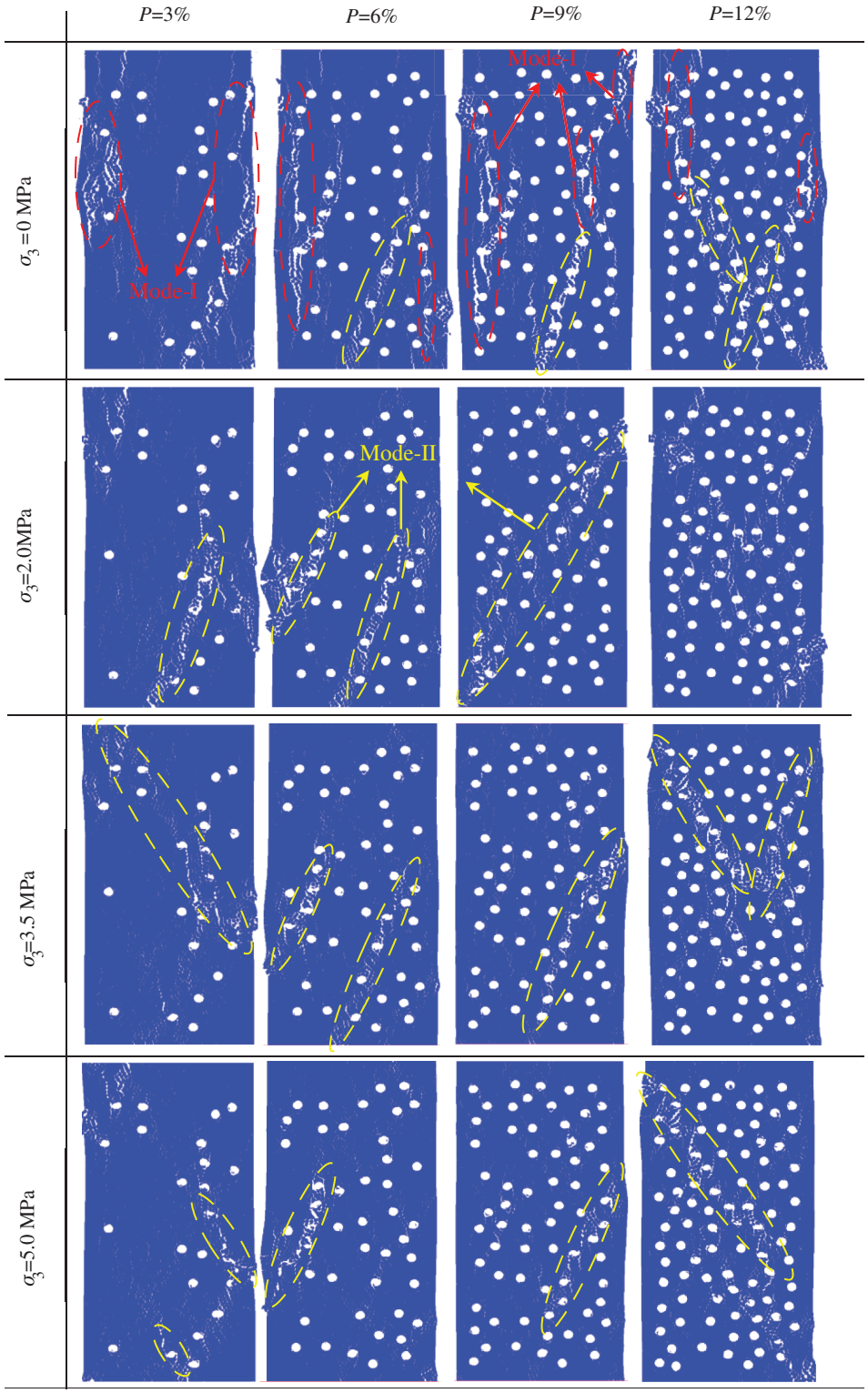

Figure 9: Failure patterns of multi-holed coal specimens

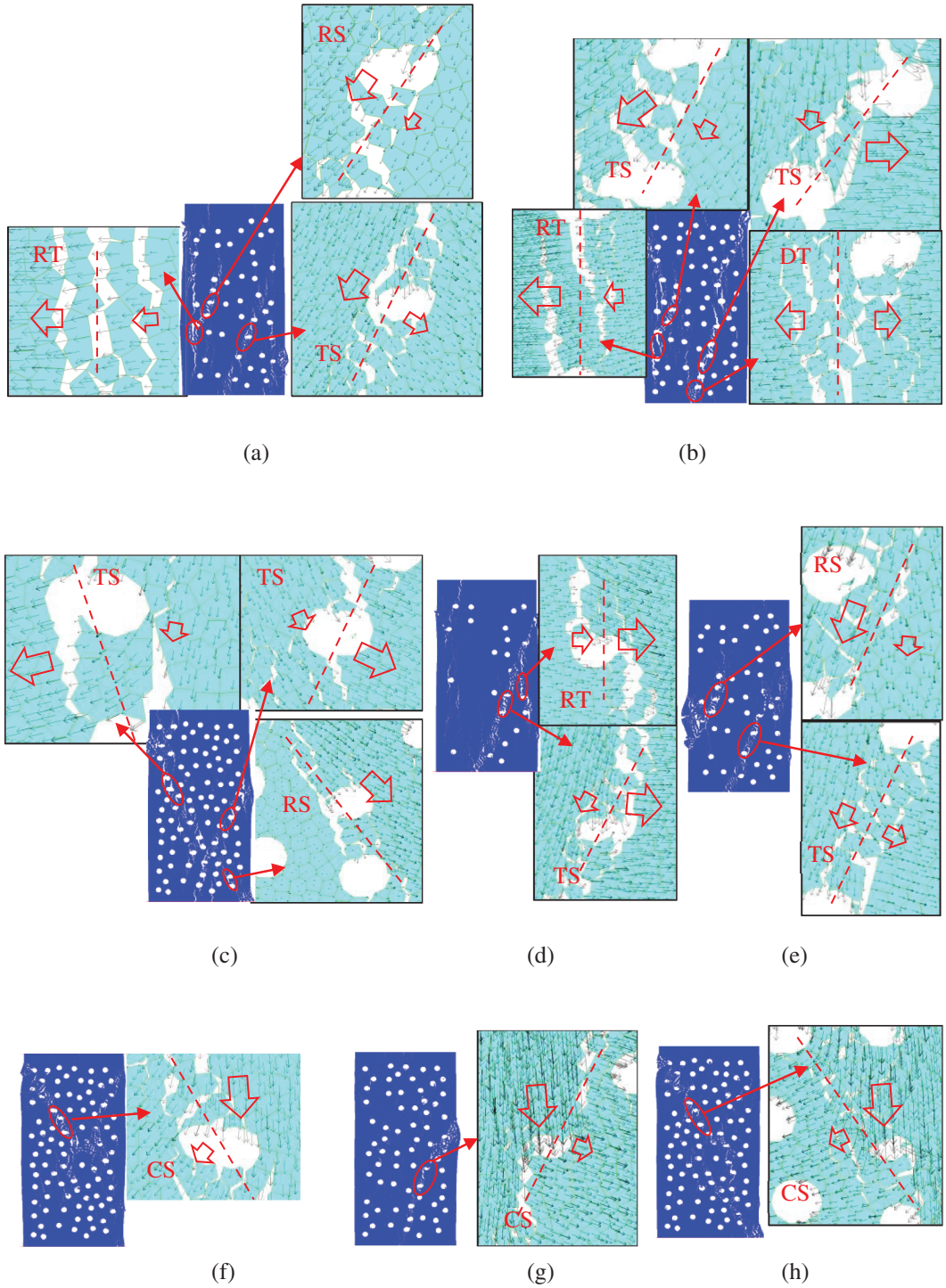

Figure 10: Mesoscopic displacement fields of blocks on both sides of fracture planes. (a) 6%—0.0 MPa. (b) 9%—0.0 MPa. (c) 12%—0.0 MPa. (d) 3%—0.5 MPa. (e) 6%—2.0 MPa. (f) 12%—3.5 MPa. (g) 9%—3.5 MPa. (h) 12%—5.0 MPa

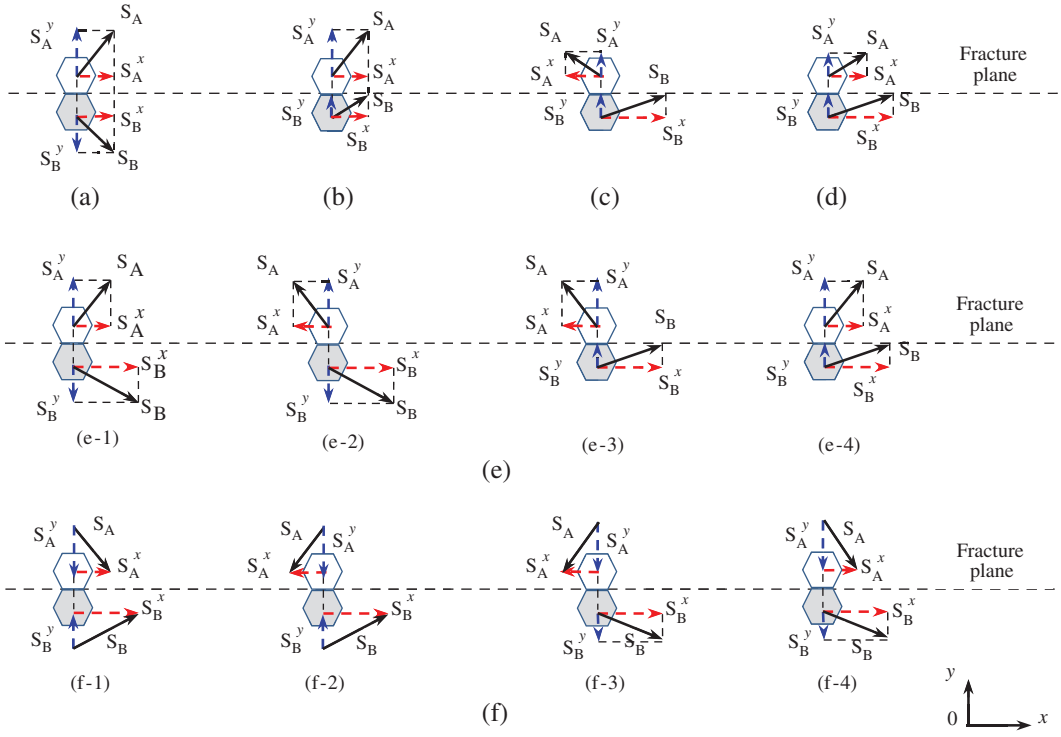

Figure 11: Six types of displacement relationships between blocks in UDEC. (a) Direct tension (DT). (b) Relative tension (DT). (c) Direct shear (DS). (d) Relative shear (RS). (e) Tensile shear (TS). (f) Compressive shear (CS)

1. Direct tension fracture (DT). S_A^y and S_B^y are in the opposite direction, which directly result in blocks separation along normal direction of fracture plane, Fig. 11a.
2. Relative tension fracture (RT). S_A^y and S_B^y are in the same direction (if y-direction) and S_A^y is larger than S_B^y, which indirectly result in blocks separation along normal direction of fracture plane, Fig. 11b.
3. Direct shear fracture (DS). S_A^x and S_B^x are in the opposite direction, which directly result in blocks slipping along tangential direction of fracture plane, Fig. 11c.
4. Relative shear fracture (RS). S_A^x and S_B^x are in the same direction but different magnitude, which indirectly result in blocks slipping along tangential direction of fracture plane, Fig. 11d.
5. Tensile shear fracture (TS). This type is a coexistence of blocks separation (DT or RT) along normal direction and slipping (DS or RS) along the fracture plane, Fig. 11e.
6. Compressive shear fracture (CS). This type is a coexistence of blocks squeeze along the normal direction and slipping along the fracture plane, Fig. 11f.

Based on the analysis of mesoscopic displacement field of blocks in Fig. 10, we can see that the splitting failure of specimens under uniaxial compression is mainly caused by RT or DT. However, shear fracture is closely related to the confining pressure. Under uniaxial compression or lower confining pressure (0.5–2.0 MPa), shear fractures are mainly controlled by RS or TS. Whereas, CS tends to be dominant when a higher confining pressure (3.5–5.0 MPa) acts.

4 Discussion

4.1 Coalescence Mechanism between Holes

Coalescence is defined as the linkage of two flaws through a combination of tensile and/or shear carcks [4,5]. Based on the numerical results, five types of coalescence modes between holes can be observed, as

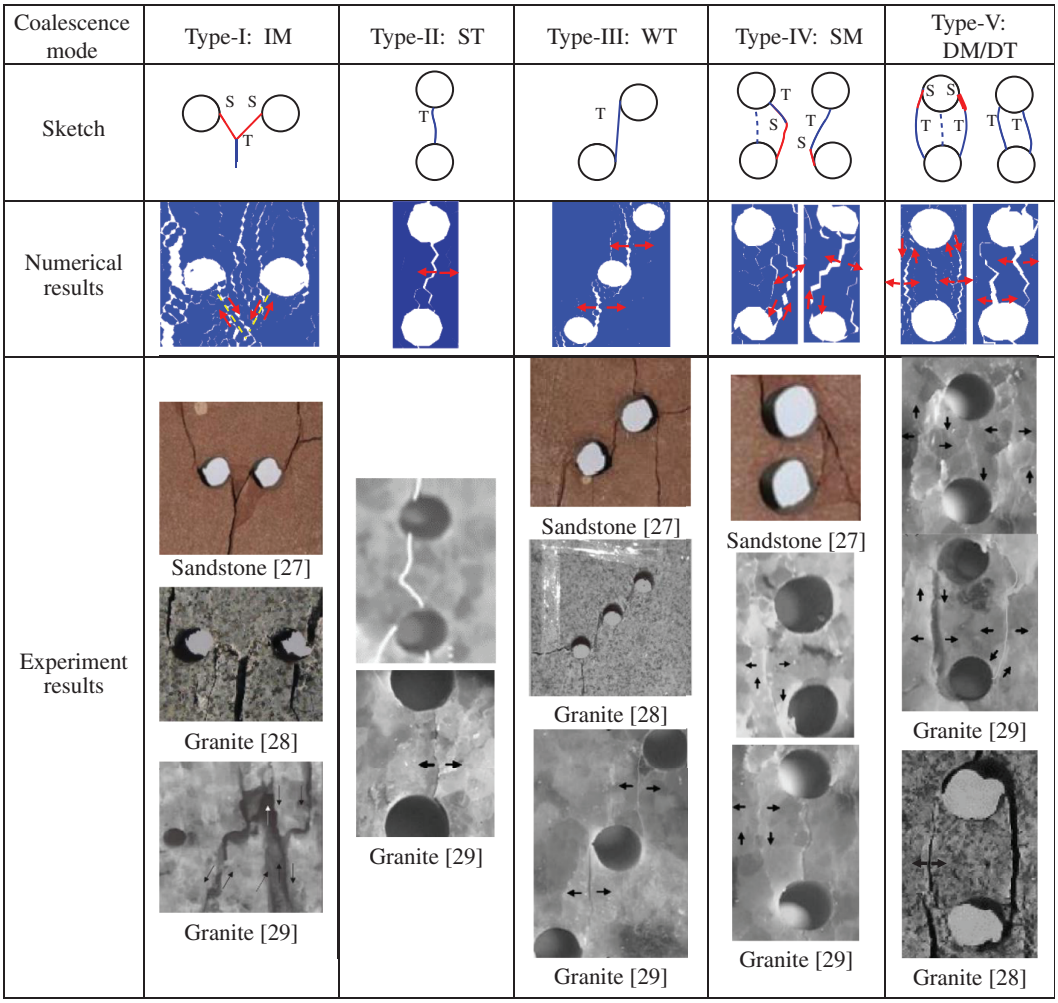

Figure 12: Five types of coalescence modes between holes

shown in Fig. 9. Each coalescence mode can match well with some previous test results, further indicating the accuracy of numerical simulation, as shown in Fig. 12.

1. Type-I: Indirect mixed crack coalescence (IM). This type usually happens between two horizontally adjacent holes. It is a combination of shear fracture originating from hole sides, and tensile cracks occurring in the material matrix.
2. Type-II: Single tensile crack coalescence (ST). This type is formed by the tensile cracks coalescence between vertically adjacent holes.
3. Type-III: Wing tensile crack coalescence (WT). The wing cracks always initiates from sides of hole and propagates near-vertically until coalescing with adjacent holes.
4. Type-IV: Single mixed carck coalescence (SM). This mode is formed by the combination of tensile crack occurring near the poles of hole and shear fractures at sides of hole. Usually, SM presents an arcuate cracking path along the rock bridge and sometimes is accompanied by ST.
5. Type-V: Double mixed crack coalescence (DM) or Double tensile crack coalescence (DT). The coalescence mode of DM or DT is in fact a coexistence of double SM or ST in the bridge area. The difference between DM and DT is the occurrence of shear fractures near sides of hole. In the

simulation results, both DM and DT can be observed. However, it may be difficult to distinguish DM and DT in experiment, because the shear cracks generated near the hole is sometimes very small and not easy to be observed.

In fact, different coalescence modes result from different interaction between holes, which is closely related to the relative locations between holes. To understand the coalescence mechanism, the effect of ligament angle (β) on the stress distribution in rock bridge areas are further researched. Fig. 13 shows the principal stress distribution in rock bridge areas with different ligament angle (β). Fig. 14 quantitatively shows the changes of principal stress magnitude with ligament angle.

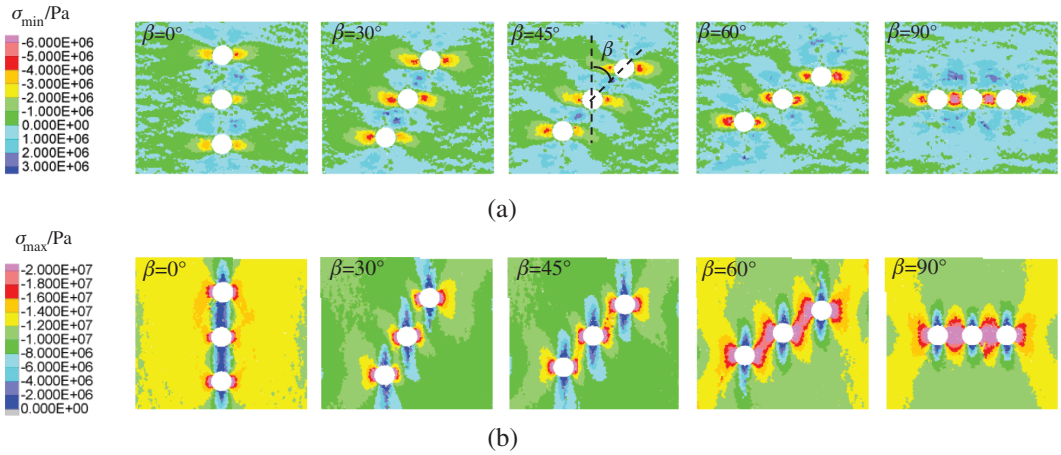

Figure 13: Principal stress distribution around holes with different ligament angle. (a) Minimum principal stress. (b) Maximum principal stress

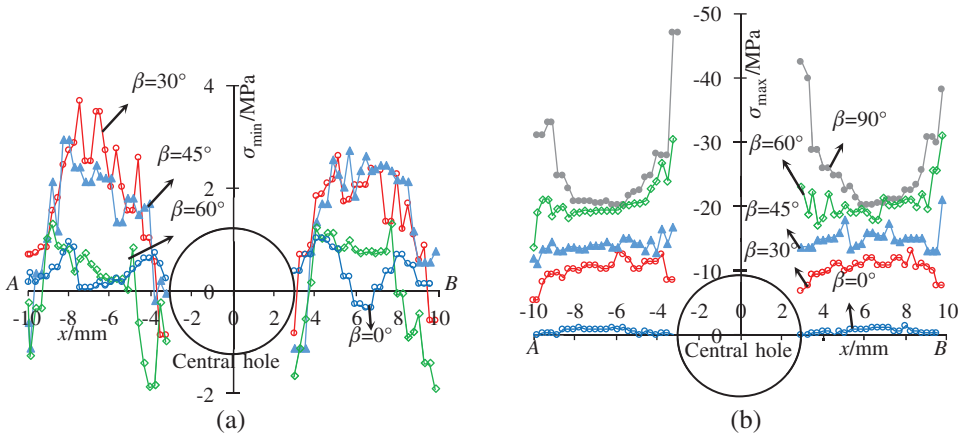

Figure 14: Changes of principal stress in the bridge area with different ligament angle. (a) Minimum principal stress. (b) Maximum principal stress

From Figs. 13 and 14, it can be found that the ligament angle (β) significantly affects the stress state in the bridge areas. When $\beta = 0°$–$45°$, the stress state of rock bridge area is dominated by tensile stress, as shown in Fig. 13a. The higher magnitude of minimum principal stress usually occurs at $\beta = 30°$–$45°$, as shown in Fig. 14a. When β increased to 60°, the tensile stress areas in rock bridge are greatly reduced. Whereas, the maximum principal stresses in rock bridge areas increase obviously with the increasing β, as shown in

Fig. 14b, showing dominate compressive stress areas at β = 60°–90°, as shown in Fig. 13b. The above indicates that the dominant stress state in rock bridges changes from tension to compression with the increasing ligament angle. Therefore, the coalescences by tensile fractures such as Type II–V usually occur with a smaller β. Whereas, the indirect coalescence (Type-I), dominated by shear fractures, mainly occurs at the rock bridges with a larger β.

4.2 Effect of P on the Bearing Area of Specimen

For the splitting failures of multi-holed specimens under uniaxial compression, it is interesting to find that most fractures are located near the boundaries of specimens. This phenomenon can be observed in detail from Fig. 15, which shows the progressive fracture process of specimen (P = 9%) under uniaxial compression. From Fig. 15, we can see that the micro-cracks firstly initiate uniformly on the north and south poles of holes (Fig. 15a). Then, those tensile cracks near the lateral boundaries rapidly expand at 0.62 UCS (Fig. 15b) and get coalescences from 0.87 UCS (Fig. 15c) to UCS (Fig. 15d). Eventually, a relatively intact region is retained in the core area of multi-holed specimen, i.e., Core Bearing Region (CBR). Two reasons may be responsible for the existence of CBR in multi-holed specimen: (1) In the core area, the compressive stress superpositions between horizontally arranged holes result in many horizontal compressive bands, which may greatly suppress the vertical propagation of tensile cracks in the core region. (2) The interaction between holes and specimen boundaries could promote the propagation and coalescence of tensile cracks in the near-boundary regions [24].

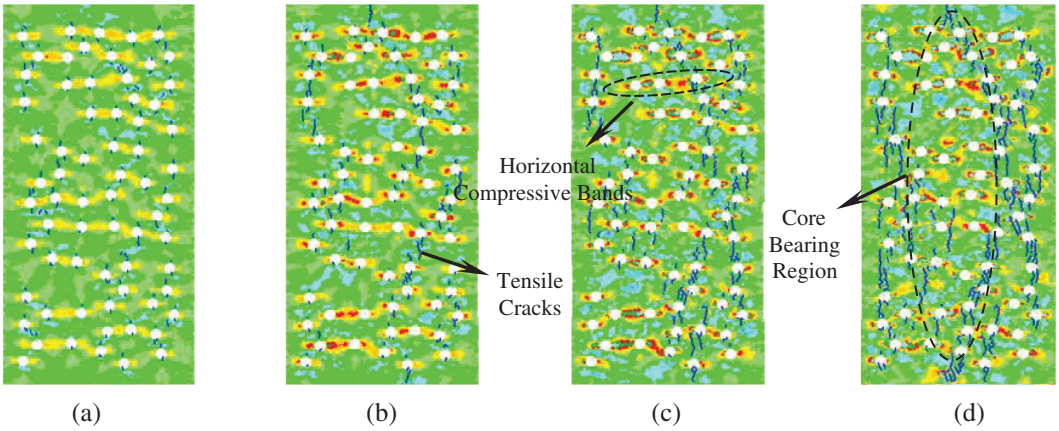

Figure 15: Fracture process of multi-hole coal specimen (P = 9%) under uniaxial compression. (a) 0.37 UCS. (b) 0.62 UCS. (c) 0.87 UCS. (d) UCS

In fact, the existence of CBR is very important for the design and support of coal pillars in underground coal mining engineering. The width of CBR is an important parameter to determine the reasonable width of coal pillars [55,56]. The simulation results in this research showed that the width of CBR may decrease with the increasing hole density, as shown in Fig. 16, indicating that a wider coal pillar will be required for the coal mass with higher macroporosity to ensure the stability of coal pillars.

4.3 Effect of P and σ_3 on Damage Behavior

The strength and deformation behavior are essentially a macroscopic performance of the accumulated microscopic damage of specimens. In this section, the number of tensile and shear cracks is used to quantitatively evaluate the tensile and shear damage of multi-holed specimens. Fig. 17 shows the effect of hole density (P) and confining pressure (σ_3) on the number of cracks (N_c) at the peak stress.

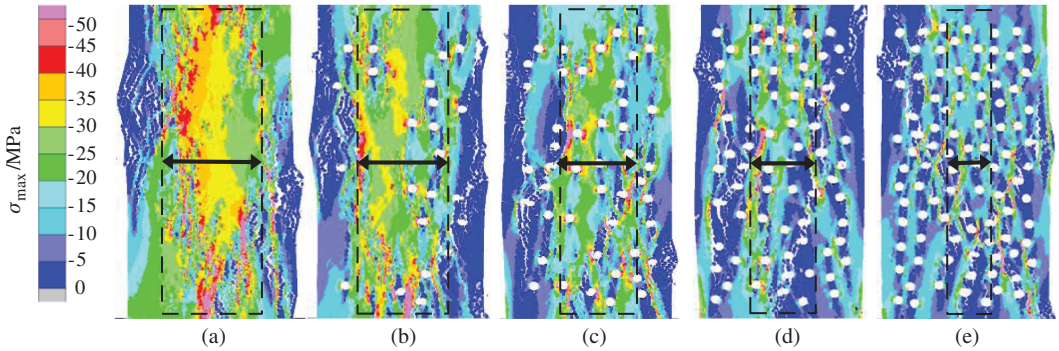

Figure 16: CBR of multi-holed specimen with different hole density. (a) Intact. (b) P = 3%. (c) P = 6%. (d) P = 9%. (e) P = 12%

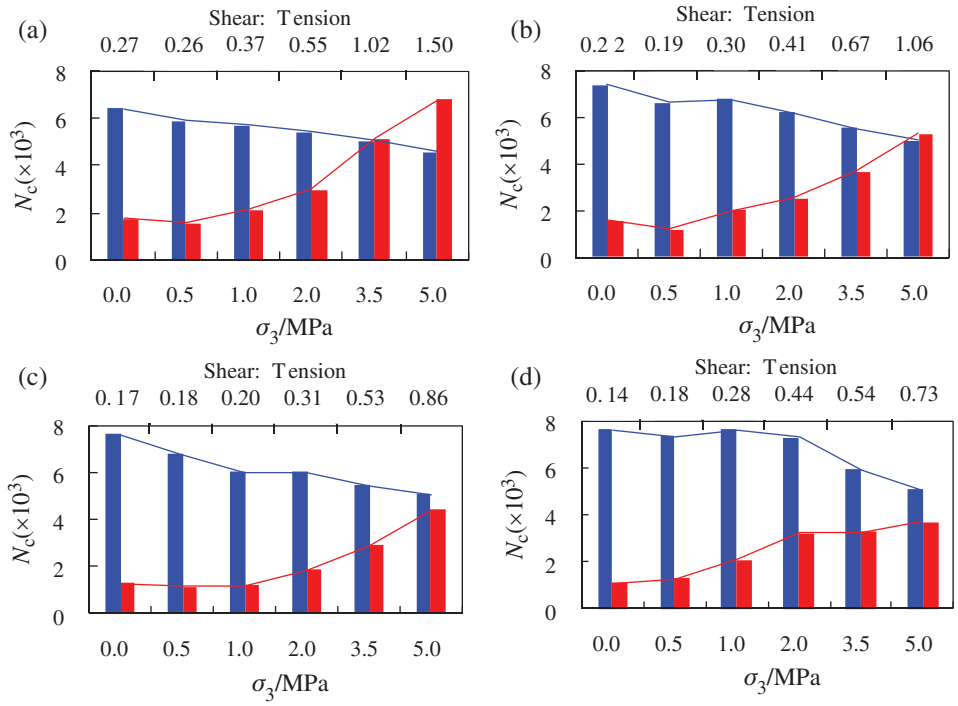

Figure 17: Changes of the number of tensile and shear cracks with different σ_3 and P. (a) P = 0%. (b) P = 3%. (c) P = 6%. (d) P = 12%

From Fig. 17, we can see that the number of shear cracks increases nonlinearly with the increasing σ_3. The increase of shear cracks tend to be larger under a higher confining pressure (2.0–5.0 MPa), especially for those with lower hole density. However, the number of tensile cracks gradually decreases with the increasing σ_3. This indicates that the increasing confining pressure will cause more shear damage and less tensile damage. Furthermore, the critical confining pressure σ_{3cr}, when the ratio of shear to tension is near 1.0, is 3.5 MPa for intact samples, then increases to near 5.0 MPa when P = 3%, and tend to be greater when P > 3%. Therefore, the σ_{3cr} tends to increase with the increasing hole density, indicating that the conversion of dominant damage from tension to shear will occurs under a higher confining pressure for specimens with a higher hole density.

The effect of confining pressure on the stress state around holes can be seen in Fig. 18, taking $P = 12\%$ as an example. From Fig. 18a, we can see that the compressive stress concentration around the hole is more intense with the increasing confining pressure, while the tension stress concentration gradually shrinks and even disappears. Simultaneously, more and more stress zones tend to be in compressive state, while the percentage of tension zones is getting smaller, as shown in Fig. 18b. Therefore, the increasing confining pressure not only strengthens the compressive stress concentration around holes but also expands the compressive stress areas, leading to a stronger tendency to shear damage.

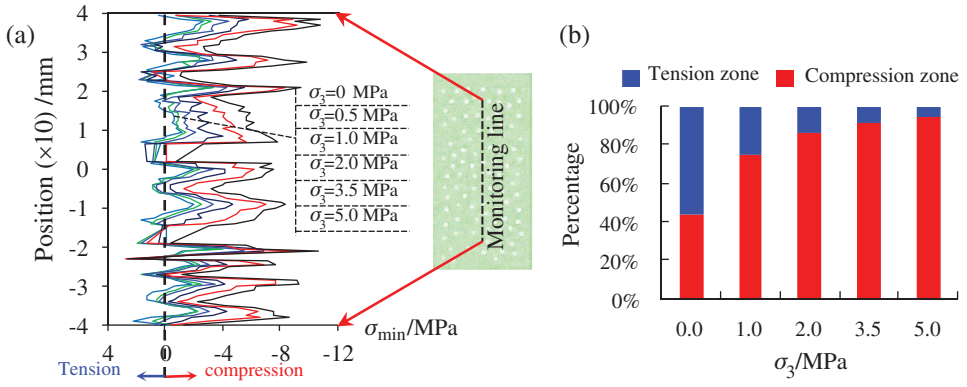

Figure 18: Changes of stress state in multi-holed coal specimens with different confining pressure (a) Minimum principal stress along monitoring line, (b) Percentage of tension and compression zones

5 Conclusions

In this research, the strength, deformation and failure behavior of multi-holed coal specimens are explored based on UDEC-GBM models. The main conclusions are as follows:

1. The strength and deformation characteristics of multi-holed coal specimens are obviously affected by hole density (P) and confining pressure (σ_3). The increasing P linearly reduces the tangent modulus and increases the degree of non-linear deformation in pre-peak stage. The strength of multi-holed coal specimens decreases exponentially with the increasing P. When $P < P_{cr}$ (critical hole density), the increasing P mainly lead to the cohesion strength loss, while leading to the frictional strength loss when $P > P_{cr}$.
2. Six types of mesoscopic displacement modes can be observed in UDEC and used to reveal the failure mechanism of multi-holed coal specimens. Splitting failure of multi-holed specimens is mainly caused by Relative Tension (RT) or Direct Tension (DT). However, shear fractures are mainly controlled by Tensile Shear (TS) or Relative Shear (RS) under lower confining pressure, or by Compressive Shear (CS) under a higher confining pressure.
3. Five types of coalescence modes between holes can be observed based on the numerical results. The coalescence modes are determined by the dominant tensile or compressive stress state of rock bridges, which is closely related to the rock bridge angle (β). With the increasing β, the dominant stress state changes from tension to compression.
4. Both hole density (P) and confining pressure (σ_3) have a significant effect on the damage behavior of multi-holed coal specimens. The increasing confining pressure not only strengthens the compressive stress concentration around holes, but also expands the compressive areas, leading to an increasing percentage of shear damage. In addition, the conversion of dominant damage from tension to shear will occurs under a higher confining pressure for specimens with higher hole density.

Funding Statement: This research was supported by China Scholarship Council (201806420027), National Natural Science Foundation of China (51904290) and Natural Science Foundation of Jiangsu Province (BK20180663).

Conflicts of Interest: The authors declare that they have no conflicts of interest to report regarding the present study.

References

1. Bobet, A., Einstein, H. H. (1998). Fracture coalescence in rock-type materials under uniaxial and biaxial compression. *International Journal of Rock Mechanics and Mining Sciences, 35(7),* 863–888. DOI 10.1016/S0148-9062(98)00005-9.
2. Sagong, M., Bobet, A. (2002). Coalescence of multiple flaws in a rock-model material in uniaxial compression. *International Journal of Rock Mechanics and Mining Sciences, 39(2),* 229–241. DOI 10.1016/S1365-1609(02)00027-8.
3. Prudencio, M., Jan, M. V. S. (2007). Strength and failure modes of rock mass models with non-persistent joints. *International Journal of Rock Mechanics and Mining Sciences, 44(6),* 890–902. DOI 10.1016/j.ijrmms.2007.01.005.
4. Park, C. H., Bobet, A. (2009). Crack coalescence in specimens with open and closed flaws: a comparison. *International Journal of Rock Mechanics and Mining Sciences, 46(5),* 819–829. DOI 10.1016/j.ijrmms.2009.02.006.
5. Park, C. H., Bobet, A. (2010). Crack initiation, propagation and coalescence from frictional flaws in uniaxial compression. *Engineering Fracture Mechanics, 77(14),* 2727–2748. DOI 10.1016/j.engfracmech.2010.06.027.
6. Chen, X., Liao, Z., Peng, X. (2012). Deformability characteristics of jointed rock masses under uniaxial compression. *International Journal of Mining Science and Technology, 22(2),* 213–221. DOI 10.1016/j.ijmst.2011.08.012.
7. Chen, X., Liao, Z. H., Peng, X. (2013). Cracking process of rock mass models under uniaxial compression. *Journal of Central South University, 20(6),* 1661–1678. DOI 10.1007/s11771-013-1660-2.
8. Zhang, X. P., Liu, Q., Wu, S., Tang, X. (2015). Crack coalescence between two non-parallel flaws in rock-like material under uniaxial compression. *Engineering Geology, 199,* 74–90. DOI 10.1016/j.enggeo.2015.10.007.
9. Yang, S. Q., Liu, X. R., Jing, H. W. (2013). Experimental investigation on fracture coalescence behavior of red sandstone containing two unparallel fissures under uniaxial compression. *International Journal of Rock Mechanics and Mining Sciences, (63),* 82–92. DOI 10.1016/j.ijrmms.2013.06.008.
10. Huang, D., Gu, D., Yang, C., Huang, R., Fu, G. (2016). Investigation on mechanical behaviors of sandstone with two preexisting flaws under triaxial compression. *Rock Mechanics and Rock Engineering, 49(2),* 375–399. DOI 10.1007/s00603-015-0757-3.
11. Li, Y. P., Chen, L. Z., Wang, Y. H. (2005). Experimental research on pre-cracked marble under compression. *International Journal of Solids and Structures, 42(9–10),* 2505–2516. DOI 10.1016/j.ijsolstr.2004.09.033.
12. Wong, L. N. Y., Einstein, H. H. (2009). Crack coalescence in molded gypsum and Carrara marble: part 1—macroscopic observations and interpretation. *Rock Mechanics and Rock Engineering, 42(3),* 475–511. DOI 10.1007/s00603-008-0002-4.
13. Wong, L. N. Y., Einstein, H. H. (2009). Crack coalescence in molded gypsum and Carrara marble: part 2—microscopic observations and interpretation. *Rock Mechanics and Rock Engineering, 42(3),* 513–545. DOI 10.1007/s00603-008-0003-3.
14. Yin, P., Wong, R. H. C., Chau, K. T. (2014). Coalescence of two parallel pre-existing surface cracks in granite. *International Journal of Rock Mechanics and Mining Sciences, 68,* 66–84. DOI 10.1016/j.ijrmms.2014.02.011.
15. Yang, S. Q., Huang, Y. H. (2017). An experimental study on deformation and failure mechanical behavior of granite containing a single fissure under different confining pressures. *Environmental Earth Sciences, 76(10),* 364. DOI 10.1007/s12665-017-6696-4.

16. Damjanac, B., Board, M., Lin, M., Kicker, D., Leem, J. (2007). Mechanical degradation of emplacement drifts at Yucca Mountain—a modeling case study: part II—lithophysal rock. *International Journal of Rock Mechanics and Mining Sciences, 44(3),* 368–399. DOI 10.1016/j.ijrmms.2006.07.010.
17. Bai, Q. S., Tu, S. H., Zhang, C. (2016). DEM investigation of the fracture mechanism of rock disc containing hole (s) and its influence on tensile strength. *Theoretical and Applied Fracture Mechanics, 86,* 197–216. DOI 10.1016/j.tafmec.2016.07.005.
18. Yang, S. Q., Huang, Y. H., Tian, W. L., Zhu, J. B. (2017). An experimental investigation on strength, deformation and crack evolution behavior of sandstone containing two oval flaws under uniaxial compression. *Engineering Geology, 217,* 35–48. DOI 10.1016/j.enggeo.2016.12.004.
19. Li, H., Li, H., Gao, B., Wang, W., Liu, C. (2017). Study on pore characteristics and microstructure of sandstones with different grain sizes. *Journal of Applied Geophysics, 136,* 364–371. DOI 10.1016/j.jappgeo.2016.11.015.
20. Yang, Z., Xia, Y., Li, M., Ma, Z., Xing, Y. et al. (2019). Effects of pore compression pretreatment on the flotation of low-rank coal. *Fuel, 239,* 63–69. DOI 10.1016/j.fuel.2018.10.145.
21. Zhou, S., Liu, D., Cai, Y., Yao, Y., Li, Z. (2017). 3D characterization and quantitative evaluation of pore-fracture networks of two Chinese coals using FIB-SEM tomography. *International Journal of Coal Geology, 174,* 41–54. DOI 10.1016/j.coal.2017.03.008.
22. Lajtai, E. Z., Carter, B. J., Duncan, E. S. (1991). Mapping the state of fracture around cavities. *Engineering Geology, 31(3–4),* 277–289. DOI 10.1016/0013-7952(1)90012-A.
23. Martin, C. D. (1997). Seventeenth Canadian geotechnical colloquium: the effect of cohesion loss and stress path on brittle rock strength. *Canadian Geotechnical Journal, 34(5),* 698–725. DOI 10.1139/t97-030.
24. Wong, R. H. C., Lin, P., Tang, C. A. (2006). Experimental and numerical study on splitting failure of brittle solids containing single pore under uniaxial compression. *Mechanics of Materials, 38(1–2),* 142–159. DOI 10.1016/j.mechmat.2005.05.017.
25. Li, D., Zhu, Q., Zhou, Z., Li, X., Ranjith, P. G. (2017). Fracture analysis of marble specimens with a hole under uniaxial compression by digital image correlation. *Engineering Fracture Mechanics, 183,* 109–124. DOI 10.1016/j.engfracmech.2017.05.035.
26. Zeng, W., Yang, S. Q., Tian, W. L. (2018). Experimental and numerical investigation of brittle sandstone specimens containing different shapes of holes under uniaxial compression. *Engineering Fracture Mechanics, 200,* 430–450. DOI 10.1016/j.engfracmech.2018.08.016.
27. Zhu, T. T., Jing, H. W., Su, H. J., Yin, Q., Du, M. R. (2015). Mechanical behavior of sandstone containing double circular cavities under uniaxial compression. *Chinese Journal of Geotechnical Engineering, 37(6),* 1047–1056.
28. Huang, Y. H., Yang, S. Q., Ranjith, P. G., Zhao, J. (2017). Strength failure behavior and crack evolution mechanism of granite containing pre-existing non-coplanar holes: experimental study and particle flow modeling. *Computers and Geotechnics, 88,* 182–198. DOI 10.1016/j.compgeo.2017.03.015.
29. Lin, P., Wong, R. H., Tang, C. A. (2015). Experimental study of coalescence mechanisms and failure under uniaxial compression of granite containing multiple holes. *International Journal of Rock Mechanics and Mining Sciences, 77,* 313–327. DOI 10.1016/j.ijrmms.2015.04.017.
30. Martin, R. J., Price, R. H., Boyd, P. J., Noel, J. S. (1994). Bulk and mechanical properties of the Paintbrush Tuff recovered from borehole USW NRG-6. *Data Report: Sandia National Laboratories Report SAND93-4020,* 9.
31. Martin, R. J., Boyd, P. J., Noel, J. S., Price, R. H. (1995). Bulk and mechanical properties of the Paintbrush Tuff recovered from borehole USW NRG-7/7A: data report. Yucca Mountain Site Characterization Project (No. SAND-94-1996). Sandia National Labs, Albuquerque, NM (USA).
32. Avar, B. B., Hudyma, N., Karakouzian, M. (2003). Porosity dependence of the elastic modulus of lithophysae-rich tuff: numerical and experimental investigations. *International Journal of Rock Mechanics and Mining Sciences, 40 (6),* 919–928. DOI 10.1016/S1365-1609(03)00074-1.
33. Hudyma, N., Avar, B. B., Karakouzian, M. (2004). Compressive strength and failure modes of lithophysae-rich Topopah Spring Tuff specimens and analog models containing cavities. *Engineering Geology, 73(1–2),* 179–190. DOI 10.1016/j.enggeo.2004.01.003.

34. Price, R. H. (2004). The mechanical properties of lithophysal tuff: laboratory experiments. YMP Project Report TDR-EBS-MD-000027 Rev, Las Vegas, NV: Bechtel-SAIC Company.
35. Avar, B. B., Hudyma, N. W. (2007). Observations on the influence of lithophysae on elastic (Young's) modulus and uniaxial compressive strength of Topopah Spring Tuff at Yucca Mountain. *International Journal of Rock Mechanics and Mining Sciences, 44(2),* 266–270. DOI 10.1016/j.ijrmms.2006.06.003.
36. Jizba, D. L. (1991). *Mechanical and acoustical properties of sandstones and shales (Ph.D. Thesis)*. Stanford University, Stanford, CA, USA.
37. Palchik, V. (1999). Influence of porosity and elastic modulus on uniaxial compressive strength in soft brittle porous sandstones. *Rock Mechanics and Rock Engineering, 32(4),* 303–309. DOI 10.1007/s006030050050.
38. Baud, P., Wong, T. F., Zhu, W. (2014). Effects of porosity and crack density on the compressive strength of rocks. *International Journal of Rock Mechanics and Mining Sciences, 67,* 202–211. DOI 10.1016/j.ijrmms.2013.08.031.
39. Cundall, P. A., Strack, O. D. (1979). A discrete numerical model for granular assemblies. *Geotechnique, 29(1),* 47–65. DOI 10.1680/geot.1979.29.1.47.
40. Zhang, Y. C., Jiang, Y. J., Tang, X. J., Chen, M., Shi, X. S. (2020). Cracking behavior and local stress characteristics around the opening surrounded by two intermittent joints: experiment and numerical simulation. *Comptes Rendus. Mécanique, 348(1),* 33–61. DOI 10.5802/crmeca.4.
41. Wang, X., Yuan, W., Yan, Y. T., Zhang, X. (2020). Scale effect of mechanical properties of jointed rock mass: a numerical study based on particle flow code. *Geomechanics and Engineering, 21(3),* 259–268.
42. Wu, N., Liang, Z. Z., Zhou, J. R., Zhang, Y. Z. (2020). Energy evolution characteristics of coal specimens with preformed holes under uniaxial compression. *Geomechanics and Engineering, 20(1),* 55–66.
43. Christianson, M., Board, M., Rigby, D. (2006). UDEC simulation of triaxial testing of lithophysal tuff. *Golden Rocks 2006, The 41st US Symposium on Rock Mechanics (USRMS)*. American Rock Mechanics Association, Golden, CO.
44. Kazerani, T., Zhao, J. (2010). Micromechanical parameters in bonded particle method for modelling of brittle material failure. *International Journal for Numerical and Analytical Methods in Geomechanics, 34(18),* 1877–1895. DOI 10.1002/nag.884.
45. Lan, H., Martin, C. D., Hu, B. (2010). Effect of heterogeneity of brittle rock on micromechanical extensile behavior during compression loading. *Journal of Geophysical Research: Solid Earth, 115(B1),* 837. DOI 10.1029/2009JB006496.
46. Gao, F., Stead, D., Elmo, D. (2016). Numerical simulation of microstructure of brittle rock using a grain-breakable distinct element grain-based model. *Computers and Geotechnics, 78,* 203–217. DOI 10.1016/j.compgeo.2016.05.019.
47. Fan, J., Xie, H., Chen, J., Jiang, D., Li, C. et al. (2020). Preliminary feasibility analysis of a hybrid pumped-hydro energy storage system using abandoned coal mine goafs. *Applied Energy, 258,* 114007. DOI 10.1016/j.apenergy.2019.114007.
48. Fan, J., Liu, W., Jiang, D., Chen, J., Tiedeu, W. N. et al. (2018). Thermodynamic and applicability analysis of a hybrid CAES system using abandoned coal mine in China. *Energy, 157,* 31–44. DOI 10.1016/j.energy.2018.05.107.
49. Itasca Consulting Group Inc. (2014). *UDEC (Universal Distinct Element Code), Version 6.0 Software*. Minneapolis, USA: Itasca Consulting Group Inc.
50. ISRM. (1979). Suggested methods for determining the uniaxial compressive strength and deformability of rock materials. *International Journal of Rock Mechanics and Mining Sciences & Geomechanics Abstracts, 16,* 135–140.
51. Zang, C., Chen, M., Zhang, G., Wang, K., Gu, D. (2020). Research on the failure process and stability control technology in a deep roadway: numerical simulation and field test. *Energy Science & Engineering,* 1–14.
52. Gao, F., Kang, H. (2017). Experimental study on the residual strength of coal under low confinement. *Rock Mechanics and Rock Engineering, 50(2),* 285–296. DOI 10.1007/s00603-016-1120-z.
53. Kovari, K., Tisa, A., Einstein, H. H., Franklin, J. A. (1983). Suggested methods for determining the strength of rock materials in triaxial compression: revised version. *International Journal of Rock Mechanics and Mining Sciences & Geomechanics Abstracts, 20(6),* 285–290. DOI 10.1016/0148-9062(83)90598-3.

54. Martin, C. D., Chandler, N. A. (1994). The progressive fracture of Lac du Bonnet granite. *International Journal of Rock Mechanics and Mining Sciences & Geomechanics Abstracts, 31(6),* 643–659. DOI 10.1016/0148-9062(94)90005-1.

55. Li, W., Bai, J., Peng, S., Wang, X., Xu, Y. (2015). Numerical modeling for yield pillar design: a case study. *Rock Mechanics and Rock Engineering, 48(1),* 305–318. DOI 10.1007/s00603-013-0539-8.

56. Zhang, G. C., He, F. L., Jia, H. G., Lai, Y. H. (2017). Analysis of gateroad stability in relation to yield pillar size: a case study. *Rock Mechanics and Rock Engineering, 50(5),* 1263–1278. DOI 10.1007/s00603-016-1155-1.